

Without Paired Labeled Data: An End-to-End Self-Supervised Paradigm for UAV-View Geo-Localization

Zhongwei Chen, Zhao-Xu Yang, Hai-Jun Rong

Abstract—UAV-View Geo-Localization (UVGL) aims to ascertain the precise location of a UAV by retrieving the most similar GPS-tagged satellite image. However, existing methods predominantly rely on supervised learning paradigms that necessitate annotated paired data for training, which incurs substantial annotation costs and impedes large-scale deployment. To overcome this limitation, we propose the Dynamic Memory-Driven and Neighborhood Information Learning (DMNIL) network, a lightweight end-to-end self-supervised framework for UAV-view geo-localization. The DMNIL framework utilizes a dual-path clustering-based contrastive learning architecture as its baseline to model intra-view structural relationships, enhancing feature consistency and discriminability. Additionally, a dynamic memory-driven hierarchical learning module is proposed to progressively mine local and global information, reinforcing multi-level feature associations to improve model robustness. To bridge the domain gap between UAV and satellite views, we design an information-consistent evolutionary learning mechanism that systematically explores latent correlations within intra-view neighborhoods and across cross-view domains, ultimately constructing a unified cross-view feature representation space. Extensive experiments on three benchmarks (University-1652, SUES-200, and DenseUAV) demonstrate that DMNIL achieves competitive performance against state-of-the-art supervised methods while maintaining computational efficiency. Notably, this superiority is attained without relying on paired training data, underscoring the framework’s practicality for real-world deployment. Codes will be released soon.

Index Terms—UAV-View Geo-Localization, Unsupervised Learning, Contrastive Learning.

I. INTRODUCTION

UAV-VIEW Geo-Localization (UVGL) aims to accurately infer the geographic location of a query image by retrieving reference images captured from different platforms[1]. In GPS-denied environments, aligning drone-captured near-ground perspective images with GPS-tagged satellite images enables precise geo-localization of scenes. This capability is essential for various applications, including autonomous navigation, disaster response, and surveillance.

This paper is submitted for review on February 18, 2025. This work was supported in part by the Key Research and Development Program of Shaanxi, PR China (No. 2023-YGBY-235), the National Natural Science Foundation of China (No. 61976172 and No. 12002254), Major Scientific and Technological Innovation Project of Xianyang, PR China (No. L2023-ZDKJ-JSGG-GY-018). (Corresponding author: Zhao-Xu Yang and Hai-Jun Rong)

Zhongwei Chen, Zhao-Xu Yang and Hai-Jun Rong are with the State Key Laboratory for Strength and Vibration of Mechanical Structures, Shaanxi Key Laboratory of Environment and Control for Flight Vehicle, School of Aerospace Engineering, Xi’an Jiaotong University, Xi’an 710049, PR China (e-mail: ISChenawei@stu.xjtu.edu.cn; yangzhx@xjtu.edu.cn; hjrong@mail.xjtu.edu.cn).

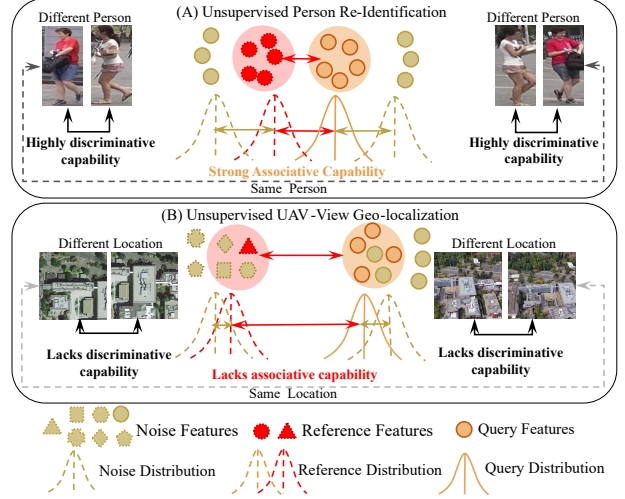


Fig. 1. (A) UReID tasks, in which intra-class variations are relatively small while inter-class differences are pronounced, facilitating robust feature discrimination.(B) UUVGL tasks, by contrast, exhibit significantly larger feature discrepancies for the same physical location due to differences in imaging conditions and viewpoints, as well as increased feature ambiguity across distinct locations arising from the spatial continuity in the captured environment.

However, existing UVGL methods adopt supervised learning frameworks that require explicitly paired UAV-satellite image datasets for training[2], [3], [4]. While achieving empirical success, these approaches face two fundamental limitations: 1) The labor-intensive annotation of pixel-level or instance-level UAV-satellite pairs incurs prohibitive scalability costs[5], and 2) Vast repositories of unpaired and unlabeled cross-view imagery remain unexploited due to the dependency on supervision. More critically, when deployed in unseen geographical regions or dynamic environments (e.g., urban construction sites), supervised models necessitate exhaustive data re-annotation to adapt to domain shifts, severely hindering real-world applicability. Considering these limitations, we aim to explore an unsupervised approach to UAV-view geo-localization (UUVGL), a paradigm that leverages self-supervised learning to autonomously discover latent cross-view correlations from large-scale unannotated data.

Although the label-free UUVGL approach demonstrates promising potential, it presents substantially greater challenges compared to other unsupervised image retrieval tasks, such as unsupervised person re-identification (UReID)[6], as illustrated in Fig.1. The UUVGL paradigm must address two

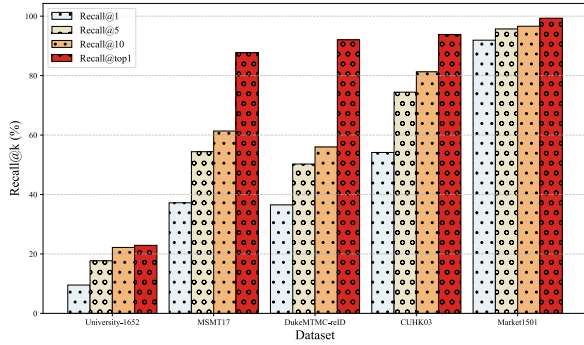


Fig. 2. Recall@k performance of ConvNeXt-Tiny[7], using pre-trained weights from ImageNet-22k[8], for direct retrieval tests on the University-1652[9] UVGL benchmark and the mainstream ReID benchmarks, including MSMT17[10], DukeMTMC-reID[11], CUHK03[12], and Market1501[13].

critical issues: 1) cross-view geometric distortions caused by significant altitude discrepancies between drone (low-altitude) and satellite (high-altitude) imaging perspectives, and 2) feature domain shifts induced by viewpoint variations. Furthermore, the inherent spatial continuity of geographical landscapes results in near-identical visual characteristics among adjacent regions, exacerbating the difficulty of discriminative location identification. As demonstrated in Fig.2, benchmark evaluations of pre-trained backbone networks on mainstream UVGL and ReID datasets reveal that initiating data relationship mining in UUVGL without annotated supervision poses considerably more challenging optimization landscapes.

In recent years, unsupervised image retrieval (UIR) [14], [15], [16] has advanced significantly, offering valuable insights for UUVGL. Broadly, existing UIR methods fall into two main categories: unsupervised domain adaptation [17] and fully unsupervised approaches [18], [19], [20]. The former still relies on labeled data in the source domain, restricting its applicability in fully unsupervised scenarios. In this paper, we focus on purely unsupervised UVGL and therefore do not provide a detailed discussion of unsupervised domain adaptation, although our method can be readily extended to accommodate such settings.

Fully UIR methods are primarily divided into two categories: image style transfer[21], [22], [23] and clustering-based pseudo-label generation[24], [25], [26]. Style transfer methods employ GANs [27] to bridge domain gaps by transforming source-domain images into the target style. However, these methods heavily depend on the quality of the generated images, which can easily introduce noise and fail to mine the complex relationships between samples in the target domain. Consequently, they do not fully exploit the inter-class separability in the target domain. In UUVGL tasks, style transfer methods struggle to address the imaging and spatial distribution differences between drone and satellite images and they incur significant training time and computational costs. Clustering-based pseudo-label generation methods assign pseudo-labels using algorithms such as DBSCAN [28] and K-means [29]. Yet, their effectiveness is highly dependent on the quality of the pseudo-labels. In UUVGL tasks, the spatial continuity of geographic environments and pronounced

cross-view differences make feature discrimination difficult, rendering pseudo-label generation susceptible to noise. Although confidence filtering [30] can alleviate some issues, the scarcity of high-confidence samples due to view differences increases the risk of overfitting and limits generalization. Furthermore, while cluster-contrast techniques are integrated to mitigate intra-cluster inconsistencies, they do not adequately address feature variations and dynamic changes across views, particularly under significant scale and perspective variations.

To address the aforementioned issues, we propose an end-to-end self-supervised framework named Dynamic Memory-Driven and Neighborhood Information Learning(DMNIL), which achieves UVGL without the need for paired training data. Specifically, the DMNIL leverages the ConvNeXt-Tiny architecture [7] for extracting coarse-grained features, adopting a dual-path cluster-based contrastive learning method [31], [32] as the baseline. Furthermore, it integrates two key modules: Dynamic Hierarchical Memory Learning (DHML) and Information Consistency Evolution Learning (ICEL). The DHML leverages the relationship between short-term and long-term memory to adaptively model intra-class feature dynamics within the same view, thereby enhancing the consistency of dynamic feature representations. The ICEL constructs a neighborhood-driven dynamic constraint mechanism based on feature distribution, integrating neighborhood consistency constraints with mutual information optimization. This module guides both intra-view and cross-view features to form consistent representations in high-dimensional feature space, effectively capturing the latent structure and mapping relationships of cross-view features. Additionally, a pseudo-label enhancement(PLE) mechanism is introduced to improve the reliability of pseudo-labels, enabling efficient self-supervised feature learning and optimization. Ultimately, we obtain a robust representation, effectively mitigating the cross-view discrepancy under unsupervised conditions. The main contributions can be summarized as follows:

- We propose a self-supervised end-to-end framework for UVGL that unifies feature representations through dynamic hierarchical clustering association and consistency information constraints. Without paired training data, this framework learns the latent consistency and shared feature mappings.
- We propose a novel dynamic memory hierarchical learning module tailored for UVGL, which adaptively explores intra-class viewpoint dynamics and contextual information, reinforcing consistent intra-class representations.
- we propose an information consistency evolution learning module that leverages neighborhood dynamic constraints and mutual information optimization to enhance shared information among features. This module dynamically establishes intra-class and inter-class neighbor learning, capturing potential mappings within and across viewpoints.
- Extensive experiments demonstrate that our framework, utilizing only a lightweight backbone, achieves state-of-the-art performance on three UVGL benchmark datasets, outperforming even certain supervised methods.

II. RELATED WORKS

In this section, we provide an overview of the cross-view geo-localization task and the commonly used methods in UIR, laying the theoretical foundation for UUVGL.

A. UAV View Geo-localization

The Cross-view Geo-localization (CVGL) task[33], [34], [35] focuses on image retrieval, aiming to identify matching images from a reference image database based on a given query image. This task is particularly challenging as the query and reference images are taken from different viewpoints or sensors. In the field of CVGL, numerous approaches have been proposed to tackle difficulties associated with scenarios such as based UAV view and ground view geo-localization.

UAV view geo-localization[36], [37] has made significant strides, with feature representation being crucial for cross-view tasks. LPN[38] mined fine-grained features through local pattern partitioning, while IFSs[35] enhanced representation by integrating global and local features via a multi-branch strategy. However, challenges remain in addressing spatial discrepancies and ensuring feature consistency. CAMP[34] tackled these issues with contrastive attribute mining and position-aware partitioning, while DAC[4] used domain alignment and scene consistency constraints to improve feature consistency. MEAN[2] incorporates progressive embedding diversification, global-to-local associations, and cross-domain enhanced alignment, improving feature representation and alignment under significant viewpoint and scale variations. Although recent advancements in UVGL methods, their training processes largely rely on paired annotated datasets. This heavy dependence on labeled data significantly limits their applicability in large-scale scenarios with unlabeled data. Currently, there are no effective methods to address this limitation. Therefore, we propose a self-supervised UVGL framework designed to leverage unlabeled data, thereby reducing the reliance on extensive annotations.

B. Ground View Geo-localization

Ground view geo-localization[39], [40] techniques have recently employed various methods to address challenges such as viewpoint variations and spatial misalignments. Early approaches, such as CVM-Net[41], used shared feature spaces to embed global descriptors, while GAN-based methods reduced visual discrepancies through view synthesis. However, these relied on fixed alignment, leading to overfitting and limited generalization. Recent methods introduced refinement and advanced architectures. TransGeo[42] employed attention-based zooming and sharpness-aware optimization to improve detail learning and generalization, while GeoDTR[43] disentangled geometric features to handle perspective shifts using a Transformer-based extractor. Hard negative mining strategies, such as those in Sample4Geo[39], further improved model discriminability by focusing on challenging negatives.

In recent years, to address the dependency on paired annotations between ground and satellite images, the literature has proposed an unsupervised ground view geo-localization method[30] that utilizes Correspondence-Free

Projection (CFP) to transform ground panorama images into bird's-eye-view (BEV) images, and applies CycleGAN[44] to reduce the visual discrepancies between ground and satellite images, while introducing a threshold-based dynamic pseudo-label updating mechanism. However, this explicit alignment approach has limitations in modeling the deep semantic relationships of cross-view features and heavily relies on the quality of CycleGAN, which may introduce artifacts and inconsistencies, affecting pseudo-label accuracy. While multi-stage training improves pseudo-label quality, it increases training time and computational cost, reducing the efficiency and practical applicability of the method. Additionally, this approach may struggle with generalization in cross-domain transfer or new scenarios. This issue motivates us to explore a fully end-to-end framework in CVGL methods, aimed at deeply mining the underlying structures and potential relationships of cross-view features while avoiding the computational resource consumption associated with multi-stage training.

C. Unsupervised Image Retrieval

In recent years, UIR methods have garnered significant attention primarily due to their ability to eliminate reliance on large-scale manually annotated data. These methods achieve effective retrieval by exploring the inherent latent structures within the data to learn discriminative feature representations. In UIR, clustering of data features is typically employed, with cluster assignments or cluster centers used as pseudo-labels to drive network learning. Representative works include DeepCluster [45] and DeepCluster-v2 [46], which enhance feature quality through iterative optimization involving feature extraction and K-means clustering. However, the quality of pseudo-labels significantly impacts retrieval performance, especially in cross-view and cross-modal scenarios where reliable cross-modal label mappings are essential. To address this, SDPL[47] introduces the Collaborative Ranking Association (CRA) module, which combines shallow and deep features to construct cross-modal ranking relationships, extracts reliable pseudo-labels through cross-validation of ranking results, and incorporates an intra-modal ranking smoothing mechanism to reduce noise interference, thereby significantly enhancing the quality and stability of pseudo-labels.

In contrast to clustering-based approaches, contrastive learning methods typically enhance feature discrimination by maximizing the similarity between different augmented views of the same image (positive pairs) and minimizing the similarity between different images (negative pairs). Early methods such as InstDisc[48] and AMDIM[49] primarily rely on large sample dictionaries or multi-view feature interactions to learn discriminative representations. The MoCo[50] series introduces a momentum update mechanism that maintains a continuously updated feature pool during training, effectively alleviating the dependence on negative sample diversity in small-batch training. SimCLR[51] further combines large-scale small-batch parallel training with data augmentation strategies, significantly improving the performance of contrastive learning. Cluster Contrast[31] generates clusters and their centers through initial clustering and introduces image-cluster center

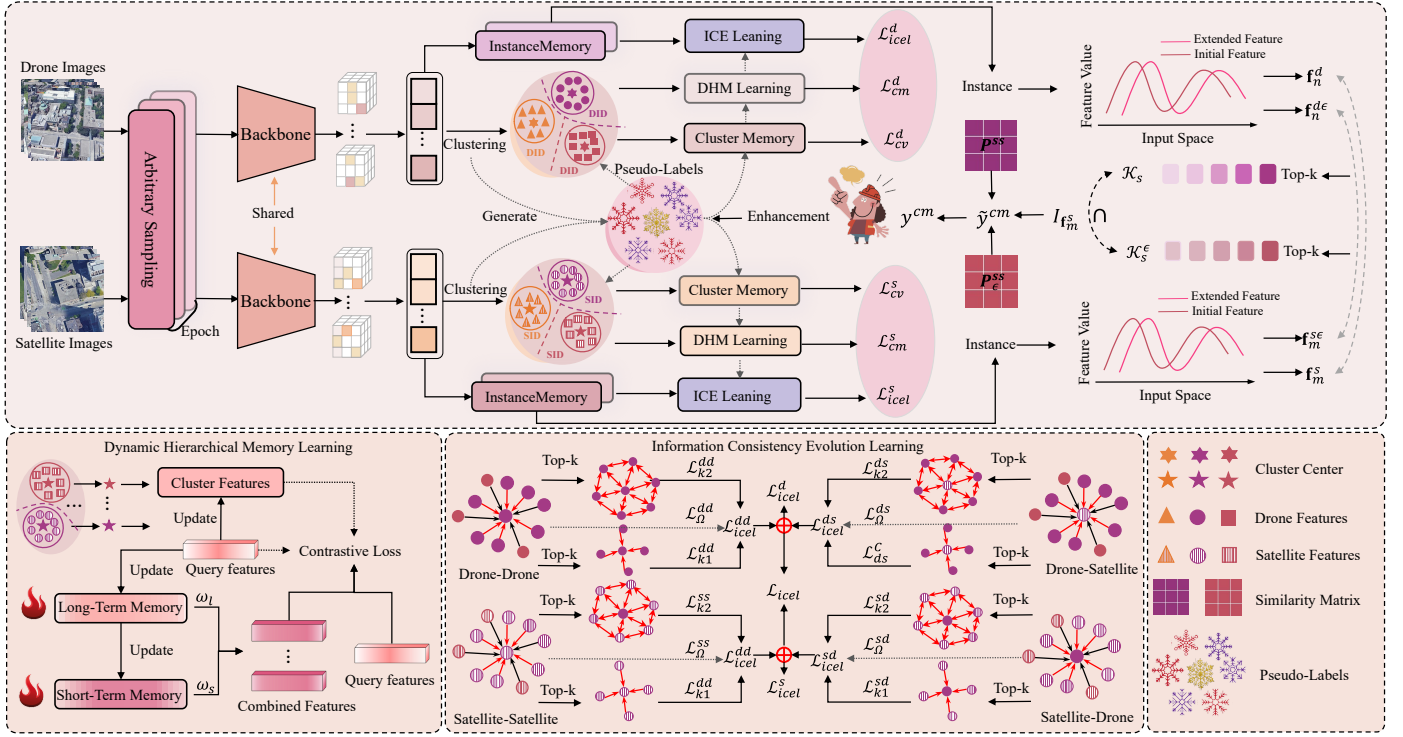


Fig. 3. The pipeline of the DMNIL framework, which includes dual-stream cluster memory contrastive learning, dynamic hierarchical memory learning, and information consistency evolution modules. The dual-stream cluster memory contrastive learning captures within-view feature representations, while the dynamic memory module models feature variations under changes in viewpoint and scale. The information consistency evolution module strengthens both intra-view and cross-view feature consistency through a neighborhood learning strategy, optimizing the learning process via pseudo-labels.

and cluster-cluster contrastive constraints within contrastive learning. The memory module continuously updates cluster centers and sample assignments, persistently optimizing cluster boundaries and member allocations to effectively address noisy samples and distribution discrepancies between cameras. In this paper, we adopt the Cluster Contrast mechanism as our baseline to implement UUVGL tasks.

III. METHOD

As illustrated in Fig.3, the DMNIL framework integrates dynamic hierarchical memory learning and information consistency evolution learning modules, along with a cross-domain pseudo-label optimization strategy. The framework employs a weight-shared dual-stream ConvNeXt-Tiny network as its backbone architecture, utilizing a cluster memory mechanism to perform contrastive learning on features extracted from different views, serving as the reference network. To mine the dynamic behavior of intra-class features under variations in viewpoint and scale, the framework establishes a collaborative relationship between short-term and long-term memory through the dynamic hierarchical memory learning module, enabling an in-depth analysis of the dynamic changes in local features and enhancing global consistency among features. Simultaneously, the information consistency evolution learning module leverages training image features stored in instance memory to design a feature distribution-based neighborhood dynamic constraint method, which combines local neighborhood consistency rules with mutual information optimization strategies. This guides both intra-view and cross-view features

to form unified representations in high-dimensional space, further uncovering the latent relationships and mapping patterns across views. Additionally, the framework incorporates a dual-joint feature-driven pseudo-label consistency enhancement mechanism to iteratively improve the reliability and semantic accuracy of pseudo-labels.

Problem Formulation: In the UUVGL task, we are given a dataset of images taken from different platforms (e.g., drones and satellites), denoted by $\{x^d, x^s\}$. Here, x^d represents drone-view images and x^s represents satellite-view images. Unlike the supervised setting, this task provides neither explicit labels nor paired matching data, meaning we do not know which drone-view images correspond to which satellite-view images, and there is no prior knowledge about location or semantic category. During model training, we apply random sampling to drone images and satellite images separately to simulate the absence of pairwise correspondences under this unsupervised setting. Our goal is to learn robust cross-view feature representations from large-scale unlabeled data under completely label-free and pair-free conditions by leveraging methods such as contrastive learning, clustering, or self-supervised learning. By utilizing these shared semantic space representations during the inference stage, the model can effectively retrieve and match images of the same location across different views, enabling accurate geo-localization without relying on any manual annotations or prior correspondence information.

A. Cluster Memory Contrastive Baseline

Cluster-based contrastive learning strategies have achieved notable success in unsupervised retrieval tasks[52]. However, in cross-geo-view tasks, due to the viewpoint imaging gap and viewpoint discrepancy, single-path cluster-based contrastive learning strategies struggle to effectively address cross-view discrepancies, lack view-specific information utilization, suffer from insufficient feature alignment, and fail to fully leverage the complementarity of different views. To address these challenges, this paper introduces a dual-path cluster-based contrastive learning method as our baseline network, which leverages two independent feature streams (drone and satellite views) for contrastive learning to enhance cross-view consistency. Specifically, drone and satellite images are fed into a shared backbone network, and then processed through their respective cluster-based contrastive learning paths to learn view-specific information and shared view features. Finally, the view-specific memories are updated via a momentum update strategy.

To facilitate the description of our method, we first introduce the notation. Let $X_d = \{x_i^d\}_{i=1}^N$ denote a set of drone images with N instances, and $X_s = \{x_i^s\}_{i=1}^M$ denote a set of satellite images with M instances. $F_d = \{f_i^d\}_{i=1}^N$ and $F_s = \{f_i^s\}_{i=1}^M$ represent the feature representations extracted by the shared feature extractor $\mathcal{F}_{backbone}$ for the drone and satellite views, respectively. q^d and q^s denote the drone query instance features and satellite query instance features extracted by the feature extractor $\mathcal{F}_{backbone}$. The processing procedure of the backbone can be described as follows.

$$\mathbf{f}_i^j = \mathcal{F}_{backbone}(x_i^j), \quad \begin{cases} i \in \{1, 2, \dots, N\}, & \text{if } j = d \\ i \in \{1, 2, \dots, M\}, & \text{if } j = s \end{cases} \quad (1)$$

Cross-View Feature Memory Initialization. At the beginning of each training epoch, the feature memories for both views are initialized. Specifically, the cluster representations of the drone view $\{\phi_1^d, \phi_2^d, \dots, \phi_K^d\}$ and the satellite view $\{\phi_1^s, \phi_2^s, \dots, \phi_L^s\}$ are stored in the drone memory dictionary \mathcal{M}_d and satellite memory dictionary \mathcal{M}_s , respectively, for view-specific memory initialization. This process can be formalized as:

$$\mathcal{M}_d \leftarrow \{\phi_1^d, \phi_2^d, \dots, \phi_K^d\} \quad (2)$$

$$\mathcal{M}_s \leftarrow \{\phi_1^s, \phi_2^s, \dots, \phi_L^s\} \quad (3)$$

$$\phi_k^d = \frac{1}{|\mathcal{H}_k^d|} \sum_{\mathbf{f}_n^d \in \mathcal{H}_k^d} \mathbf{f}_n^d \quad (4)$$

$$\phi_l^s = \frac{1}{|\mathcal{H}_l^s|} \sum_{\mathbf{f}_m^s \in \mathcal{H}_l^s} \mathbf{f}_m^s \quad (5)$$

where, $n = 1, \dots, N$, $m = 1, \dots, M$, $k = 1, \dots, K$, $l = 1, \dots, L$, $\mathcal{H}_{k(l)}^{d(s)}$ denotes the k -th cluster set in drone or satellite view, $|\cdot|$ indicates the number of instances per cluster.

Cross-View Feature Memory Updating. During the training phase, we randomly sample P distinct localization points from the training set, with each point comprising a fixed number Z of instances. This sampling strategy results in a minibatch containing a total of $P \times Z$ query images. Subsequently, the

query features extracted from the minibatch are integrated into the cluster representations via a momentum-based update mechanism. Through this approach, we iteratively update the features for both perspectives, as formalized in Eq.6 and Eq.7.

$$\phi_k^{d(\omega)} \leftarrow \alpha \phi_k^{d(\omega-1)} + (1 - \alpha) q^d \quad (6)$$

$$\phi_k^{s(\omega)} \leftarrow \alpha \phi_k^{s(\omega-1)} + (1 - \alpha) q^s \quad (7)$$

where α is the momentum updating factor. ω is the iteration number.

Cross-View Contrastive Loss. Given drone and satellite query q^d and q^s , we compute the contrastive loss for drone view and satellite view by the following equations:

$$\mathcal{L}_{cv}^d = -\log \frac{\exp(q^d \cdot \phi_+^d / \tau)}{\sum_{k=0}^K \exp(q^d \cdot \phi_k^d / \tau)} \quad (8)$$

$$\mathcal{L}_{cv}^s = -\log \frac{\exp(q^s \cdot \phi_+^s / \tau)}{\sum_{k=0}^K \exp(q^s \cdot \phi_k^s / \tau)} \quad (9)$$

where, τ denotes the temperature hyper-parameter. The cluster centroids $\phi_{k(l)}^{d(s)}$ are utilized as feature vectors at the cluster level to compute the distances between the query instance $q_{d(s)}$ and all clusters. Here, $\phi_+^{d(s)}$ corresponds to the positive cluster feature associated with $q_{d(s)}$.

The final optimization for baseline is denoted by the following combination:

$$\mathcal{L}_{cv} = \mathcal{L}_{cv}^d + \mathcal{L}_{cv}^s \quad (10)$$

B. Dynamic Hierarchical Memory Learning

In CVGL tasks, baseline networks can rapidly respond to local environmental changes and learn subtle differences in recent scenes. However, they are susceptible to transient noise and local anomalies, leading to instability in feature representation. Moreover, due to the complexity introduced by geographic variations, baseline networks struggle to extract globally consistent and stable features effectively. To address these challenges, we propose a Dynamic Hierarchical Memory Learning (DHML) method to achieve a balance between instantaneous adaptation and long-term stability.

Consistent with the baseline network, we construct the dynamic hierarchical memory learning in a dual-path manner, using drone feature extraction as an illustrative example. To build the long-term memory, we first construct two novel clustering memory dictionaries according to Eq.2 and Eq.3, which are used to store the short-term \mathcal{M}_d^s and long-term \mathcal{M}_d^l memories, respectively.

$$\mathcal{M}_d^s \leftarrow \{\varphi_1^{ds}, \varphi_2^{ds}, \dots, \varphi_K^{ds}\} \quad (11)$$

$$\mathcal{M}_d^l \leftarrow \{\varphi_1^{dl}, \varphi_2^{dl}, \dots, \varphi_K^{dl}\} \quad (12)$$

where, $\varphi_1^{ds}, \varphi_2^{ds}, \dots, \varphi_K^{ds}$ represent the short-term memory embeddings that encode the cluster representations of the drone view, and $\varphi_1^{dl}, \varphi_2^{dl}, \dots, \varphi_K^{dl}$ represent the long-term memory embeddings that store historically accumulated stable representations of the drone view.

Unlike the weight updating scheme in Eq.6 and Eq.7, we assign different weights to the input features and the historical

memory during the long-term memory update. Specifically, since the momentum parameter is set to 0.2 throughout this study, during the initialization of the long-term memory update we deliberately reduce the influence of the current input (i.e., the input weight is $1 - \alpha$) and amplify the influence of the historical memory (i.e., the historical weight is α) to maintain consistency and stability of the memory. The update procedure can be defined as follows:

$$\varphi_k^{dl(\omega)} \leftarrow (0.5 - \alpha)\phi_k^{dl(\omega-1)} + \alpha q_{dl} \quad (13)$$

where, q_{dl} represents the drone query instance features. This obtain a new dictionary of long-term memory .

In order to learn local input information while preserving global consistency, we further introduce an adaptive weight updating mechanism to update the long-term memory. In detail, we first compute the Euclidean distance between the current input and its corresponding long-term memory, then take the average over all samples in the batch. This average distance is then mapped to the range $[0, 1]$ via the sigmoid function, yielding an adaptive update coefficient β :

$$\beta = \sigma\left(\frac{1}{B} \sum_{i=1}^B \|q_{dl} - \phi_k^{dl(\omega-1)}\|\right) \quad (14)$$

where, B denotes the batch size and $\sigma(\cdot)$ represents the sigmoid function. The short-term memory is subsequently updated as follows:

$$\varphi_k^{ds(\omega)} \leftarrow \beta \cdot \varphi_k^{dl(\omega-1)} + (1 - \beta) \cdot \varphi_k^{ds(\omega-1)} \quad (15)$$

This adaptive updating strategy ensures that, when there is a significant deviation between the input and the short-term memory, the current input information exerts a greater influence on the long-term memory, thereby enabling a more rapid capture of scene changes. Conversely, when the deviation is small, the historical memory predominantly contributes to maintaining global consistency. Finally, the long-term and short-term memories are fused in a weighted manner to yield the combined feature φ_k^{db} representation:

$$\varphi_k^{db(\omega)} = w_l \cdot \varphi_k^{dl(\omega)} + w_s \cdot \varphi_k^{ds(\omega)} \quad (16)$$

where w_l and w_s denote the respective fusion weights. As a result, we obtain a comprehensive memory dictionary \mathcal{M}_d^{cb} that effectively integrates long-term global consistency with localized short-term adaptability, ensuring robust and stable feature representation across varying environmental conditions.

Given the drone query q^d , we compute the contrastive loss by measuring their similarity to the cluster representations maintained in the memory dictionary by the following equations:

$$\mathcal{L}_{id}^{dd} = -\log \frac{\exp(q^d \cdot \varphi_+^{db}/\tau)}{\sum_{k=0}^K \exp(q^d \cdot \varphi_k^{db}/\tau)} \quad (17)$$

where, τ denotes the temperature hyper-parameter. The combined cluster centroids ϕ_k^{db} are utilized as feature vectors at the cluster level to compute the distances between the query instance q^d and all clusters. Here, ϕ_+^{db} corresponds to the positive cluster feature associated with q^d .

To further reinforce local adaptability while maintaining stability, we integrate our proposed loss function with the baseline loss \mathcal{L}_{cv}^d , ensuring that the model effectively learns fine-grained scene variations while preserving robust global consistency. The final optimization objective is formulated as:

$$\mathcal{L}_{dhml}^d = \mathcal{L}_{cv}^d + \lambda_{cv} \mathcal{L}_{cv}^{dd} \quad (18)$$

where λ_{cv} is a trade-off parameter that controls the contribution of the \mathcal{L}_{dhml}^d . The satellite contrastive loss \mathcal{L}_{dhml}^s are obtained by the same way.

We effectively refine the feature representation by balancing cross view local adaptability and global stability by combining cross view hierarchical memory learning approach:

$$\mathcal{L}_{dhml} = \mathcal{L}_{dhml}^d + \mathcal{L}_{dhml}^s \quad (19)$$

C. Information Consistency Evolution Learning

By integrating the baseline network with the dynamic hierarchical memory learning module, the proposed framework exhibits a certain capability for cross-view consistency learning. However, both the baseline network and the dynamic hierarchical memory learning module primarily focus on intra-view feature learning, even though the drone-view and satellite-view features share a common backbone network. As a result, the deep correlations between features from different views remain insufficiently explored, limiting the model's ability to fully mitigate and bridge the challenges posed by drastic viewpoint variations.

To address this limitation, we propose an Information Consistency Evolution Learning (ICEL) module, as illustrated in Fig.3. This module leverages a threshold-based filtering and ranking-driven neighborhood selection strategy to reinforce intra-view consistency while simultaneously enabling cross-view feature alignment. By facilitating consistency evolution across views, ICEL enhances the discriminative power and relational modeling of both intra-view and cross-view feature representations, thereby improving the model's robustness in complex geo-localization scenarios.

In the ICEL module, unlike the baseline and DHML module, we employ instance-level features instead of cluster-level representations. To achieve this, we define two instance memory dictionaries, \mathcal{I}_d and \mathcal{I}_s , which store the instance features extracted by the shared feature encoder, as described in Section III-A. This process can be formally expressed as follows:

$$\mathcal{I}_d \leftarrow \{\mathbf{f}_1^d, \mathbf{f}_2^d, \dots, \mathbf{f}_N^d\} \quad (20)$$

$$\mathcal{I}_s \leftarrow \{\mathbf{f}_1^s, \mathbf{f}_2^s, \dots, \mathbf{f}_M^s\} \quad (21)$$

where \mathbf{f}_n^d and \mathbf{f}_m^s denote the drone and satellite instance features stored in memory dictionaries \mathcal{I}_d and \mathcal{I}_s , respectively.

In addition, we define the similarity between a given drone (or satellite) query $q_z^{d(s)}$ and each drone (or satellite) instance $\mathbf{f}_v^{d(s)}$ in the training set as:

$$\mathcal{S}(q_z^{d(s)}, \mathbf{f}_v^{d(s)}) = \frac{q_z^{d(s)} \cdot \mathbf{f}_v^{d(s)}}{\|q_z^{d(s)}\|_2 \|\mathbf{f}_v^{d(s)}\|_2}, \quad (22)$$

where z and v are the indices of queries and instances. Thus, we obtain intra-view similarity $\mathcal{S}(q_z^d, \mathbf{f}_v^d)$, $\mathcal{S}(q_z^s, \mathbf{f}_v^s)$ and cross-view similarity $\mathcal{S}(q_z^d, \mathbf{f}_v^s)$, $\mathcal{S}(q_z^s, \mathbf{f}_v^d)$.

Based on the instance memory dictionary and similarity computation (as shown in Fig.3), we adopt two learning modes: intra-view representation enhancement and cross-view feature association. To ensure that the learning process relies only on high-confidence neighborhood information, we introduce a neighborhood selection strategy that integrates threshold-based filtering and top- k ranking. The threshold-based filtering strategy can be defined as follows:

$$\Omega^{dd} = \left\{ \mathbf{f}_v^d \mid S(q_z^d, \mathbf{f}_v^d) > \gamma \max_{v \in \{1, \dots, N\}} S(q_z^d, \mathbf{f}_v^d) \right\} \quad (23)$$

$$\Omega^{ds} = \left\{ \mathbf{f}_v^s \mid S(q_z^d, \mathbf{f}_v^s) > \gamma \max_{v \in \{1, \dots, M\}} S(q_z^d, \mathbf{f}_v^s) \right\} \quad (24)$$

where, Ω^{dd} represents the set of drone feature instances selected as valid intra-view neighbors and Ω^{ds} denotes the set of drone feature instances that exhibit strong cross-view associations with satellite features. $\gamma \in (0, 1)$ is a predefined threshold. The Ω^{ss} and Ω^{sd} can be calculated by the same way.

Although fixed-threshold-based neighborhood selection identifies highly relevant samples, it may still yield an excessively large neighborhood due to its global filtering nature. To refine this into a more compact and discriminative set, we introduce a top- k ranking selection strategy. Specifically, we independently select the top- k_1 most relevant samples to construct a strictly filtered neighborhood, ensuring high-confidence associations, while also selecting the top- k_2 samples define an expanded neighborhood, capturing additional informative relationships. The process can be defined by:

$$\mathcal{N}_{k_1}^{dd} = \left\{ \mathbf{f}_v^d \mid v \in \arg \max_{V \subset \{1, \dots, N\}, |V|=k_1} \sum_{v \in V} S(q_z^d, \mathbf{f}_v^d) \right\} \quad (25)$$

$$\mathcal{N}_{k_1}^{ds} = \left\{ \mathbf{f}_v^s \mid v \in \arg \max_{V \subset \{1, \dots, M\}, |V|=k_1} \sum_{v \in V} S(q_z^d, \mathbf{f}_v^s) \right\} \quad (26)$$

$$\mathcal{N}_{k_2}^{dd} = \left\{ \mathbf{f}_v^d \mid v \in \arg \max_{V \subset \{1, \dots, N\}, |V|=k_2} \sum_{v \in V} S(q_z^d, \mathbf{f}_v^d) \right\} \quad (27)$$

$$\mathcal{N}_{k_2}^{ds} = \left\{ \mathbf{f}_v^s \mid v \in \arg \max_{V \subset \{1, \dots, M\}, |V|=k_2} \sum_{v \in V} S(q_z^d, \mathbf{f}_v^s) \right\} \quad (28)$$

where $\mathcal{N}_{k_1}^{dd}$, $\mathcal{N}_{k_2}^{dd}$ and $\mathcal{N}_{k_1}^{ds}$, $\mathcal{N}_{k_2}^{ds}$ denote the selected intra-view and cross-view neighborhood sets, respectively, with $\mathcal{N}_{k_1}^{dd}$ and $\mathcal{N}_{k_1}^{ds}$ containing exactly k_1 elements, and $\mathcal{N}_{k_2}^{dd}$ and $\mathcal{N}_{k_2}^{ds}$ containing exactly k_2 elements. Similarly, the neighborhood sets $\mathcal{N}_{k_1}^{ss}$, $\mathcal{N}_{k_1}^{sd}$, $\mathcal{N}_{k_2}^{ss}$, and $\mathcal{N}_{k_2}^{sd}$ can be obtained following the same selection strategy.

Based on the constructed neighborhoods, we further define three loss functions. First, within a larger-scale neighborhood, to enhance the aggregation of similar samples in both intra-view and cross-view settings, we compute the normalized similarity distribution over the selected neighborhood set and optimize it using a cross-entropy loss to maximize the

alignment between the query sample and its neighborhood samples. The intra-view $\mathcal{L}_{\Omega}^{dd}$ and cross-view $\mathcal{L}_{\Omega}^{ds}$ losses can be formulated as:

$$\mathcal{L}_{\Omega}^{dd} = -\frac{1}{N^b} \sum_{z=1}^{N^b} \sum_{v \in \Omega^{dd}} \log \frac{\exp(S(q_z^d, \mathbf{f}_v^d)/\tau)}{\sum_{v=1}^{N^{\Omega^{dd}}} \exp(S(q_z^d, \mathbf{f}_v^d)/\tau)} \quad (29)$$

$$\mathcal{L}_{\Omega}^{ds} = -\frac{1}{N^b} \sum_{z=1}^{N^b} \sum_{v \in \Omega^{ds}} \log \frac{\exp(S(q_z^d, \mathbf{f}_v^s)/\tau)}{\sum_{v=1}^{N^{\Omega^{ds}}} \exp(S(q_z^d, \mathbf{f}_v^s)/\tau)} \quad (30)$$

where N^b represents the batch size of the query q_z^d , $N^{\Omega^{dd}}$ and $N^{\Omega^{ds}}$ denote the total number of neighborhood samples within the set Ω^{dd} and Ω^{ds} .

Incorporating neighborhoods $\mathcal{N}_{k_1}^{dd}$, $\mathcal{N}_{k_2}^{dd}$ and $\mathcal{N}_{k_1}^{ds}$, $\mathcal{N}_{k_2}^{ds}$, in addition to intra-view and cross-view neighborhood contrastive losses, we introduce consistency loss and mutual information loss to enhance feature robustness and semantic alignment across views.

The consistency loss minimizes the Kullback-Leibler to enforce alignment of relative similarity distributions within the large-scale neighborhood k_2 across both intra-view and cross-view representations. This ensures that features from different modalities or viewpoints maintain a consistent neighborhood structure. The intra-view loss $\mathcal{L}_{k_2}^{dd}$ and cross-view loss $\mathcal{L}_{k_2}^{ds}$ under this consistency loss can be formulated as:

$$p_{z,v}^{dd} = \frac{\exp(S(q_z^d, \mathbf{f}_v^d))}{\sum_{v' \in \mathcal{N}_{k_2}^{dd}} \exp(S(q_z^d, \mathbf{f}_{v'}^d))} \quad (31)$$

$$p_{z,v}^{ds} = \frac{\exp(S(q_z^d, \mathbf{f}_v^s))}{\sum_{v' \in \mathcal{N}_{k_2}^{ds}} \exp(S(q_z^d, \mathbf{f}_{v'}^s))} \quad (32)$$

$$\mathcal{L}_{k_2}^{dd} = \frac{1}{B} \sum_{z=1}^B \sum_{v \in \mathcal{N}_{k_2}^{dd}} p_{z,v}^{dd} \log(k_2 \cdot p_{z,v}^{dd}) \quad (33)$$

$$\mathcal{L}_{k_2}^{ds} = \frac{1}{B} \sum_{z=1}^B \sum_{v \in \mathcal{N}_{k_2}^{ds}} p_{z,v}^{ds} \log(k_2 \cdot p_{z,v}^{ds}) \quad (34)$$

where, $p_{z,v}^{d(s)}$ is the softmax-normalized similarity distribution, v' is used for summation to normalize the similarity scores over all neighborhood samples. $\mathcal{L}_{k_2}^{ss}$ and $\mathcal{L}_{k_2}^{sd}$ can be obtained in the same way.

Finally, within a more restrictive and smaller set of k_1 neighbors, a mutual information constraint is proposed to learn fine-grained relationships between the query feature and local samples. This complements the consistency constraint described above, achieving a balance between global structural alignment and local discriminative information. Within the selected k_1 neighborhood, we first compute, for each neighbor sample $\mathbf{f}_{v_i}^{d(s)}$ (where $i = 1, \dots, k_1$), the similarity between the deep query feature q_z^d and the neighbor feature $\mathbf{f}_{v_i}^{d(s)}$ using the similarity function $S(q_z^{d(s)}, \mathbf{f}_{v_i}^{d(s)})$. Based on these similarity scores, the posterior probability for each neighbor is defined via a softmax normalization as:

$$p_i^{d(s)d(s)}(v_i | q_z^{d(s)d(s)}) = \frac{\exp(S(q_z^{d(s)}, \mathbf{f}_{v_i}^{d(s)}))}{\sum_{j=1}^R \exp(S(q_z^{d(s)}, \mathbf{f}_{v_j}^{d(s)}))} \quad (35)$$

where R denote the total number of neighborhood samples within the set \mathcal{N}_{k1}^{dd} and \mathcal{N}_{k1}^{ds} .

Therefore, the intra-view and cross-view mutual information losses \mathcal{L}_{k1}^{dd} and \mathcal{L}_{k1}^{ds} can be derived and are defined as follows:

$$\mathcal{L}_{k1}^{dd} = -\frac{1}{B} \sum_{z=1}^B \sum_{i=1}^R p_i^{dd}(v_i|q_z^d) \log \frac{p_i^{dd}(v_i|q_z^d)}{1/R} \quad (36)$$

$$\mathcal{L}_{k1}^{ds} = -\frac{1}{B} \sum_{z=1}^B \sum_{i=1}^R p_i^{ds}(v_i|q_z^d) \log \frac{p_i^{ds}(v_i|q_z^d)}{1/R} \quad (37)$$

where $p_i^{dd}(v_i|q_z^d)$ and $p_i^{ds}(v_i|q_z^d)$ represent the normalized similarity distributions over the selected R intra-view and cross-view neighbors, respectively. \mathcal{L}_{k1}^{ss} and \mathcal{L}_{k1}^{ds} can be obtain in the same way. These mutual information losses maximize the entropy of the learned feature distributions, ensuring that the query features maintain a well-separated and informative representation within their respective local neighborhoods.

For each viewpoint, the corresponding loss can be formulated as follows:

$$\mathcal{L}_{icel}^{dd} = \mathcal{L}_{\Omega}^{dd} + \lambda_{k1} \mathcal{L}_{k1}^{dd} + \lambda_{k2} \mathcal{L}_{k2}^{dd} \quad (38)$$

$$\mathcal{L}_{icel}^{ds} = \mathcal{L}_{\Omega}^{ds} + \lambda_{k1} \mathcal{L}_{k1}^{ds} + \lambda_{k2} \mathcal{L}_{k2}^{ds} \quad (39)$$

$$\mathcal{L}_{icel}^{ss} = \mathcal{L}_{\Omega}^{ss} + \lambda_{k1} \mathcal{L}_{k1}^{ss} + \lambda_{k2} \mathcal{L}_{k2}^{ss} \quad (40)$$

$$\mathcal{L}_{icel}^{sd} = \mathcal{L}_{\Omega}^{sd} + \lambda_{k1} \mathcal{L}_{k1}^{sd} + \lambda_{k2} \mathcal{L}_{k2}^{sd} \quad (41)$$

where λ_{k1} and λ_{k2} are importance adjustment factors. The final optimization for neighbor learning is denoted by the following combination:

$$\mathcal{L}_{icel} = \mathcal{L}_{icel}^d + \mathcal{L}_{icel}^s \quad (42)$$

where $\mathcal{L}_{icel}^d = \mathcal{L}_{icel}^{dd} + \mathcal{L}_{icel}^{ds}$ and $\mathcal{L}_{icel}^s = \mathcal{L}_{icel}^{ss} + \mathcal{L}_{icel}^{sd}$. The overall loss for DMNIL is denoted as:

$$\mathcal{L}_{total} = \mathcal{L}_{cv} + \mathcal{L}_{dhml} + \mathcal{L}_{icel} \quad (43)$$

D. Pseudo-Label Enhancement

In an unsupervised learning scenario, the quality of pseudo-labels exerts a decisive influence on model performance. Inspired by [47], this study proposes a pseudo-label optimization framework based on dynamic feature robustness. Specifically, small perturbations are introduced into the original feature representation to form a perturbed feature space, and the Top-K nearest neighbor consistency between the original and perturbed features is employed to identify high-confidence samples while filtering out noisy or less discriminative instances. Subsequently, leveraging the inter-sample similarity matrix in the feature space, a spatial smoothing operation is performed on the initially generated pseudo-labels, thereby enforcing local label consistency among neighboring samples.

We first employ small Gaussian noise $\epsilon_d, \epsilon_s \sim \mathcal{N}(\mathbf{0}, \sigma^2 \mathbf{I})$ into the original satellite instances feature and the original drone instances features to obtain perturbed features, which are used for more robust similarity estimation and subsequent cluster consistency evaluation. specifically:

$$\mathbf{f}_n^{d\epsilon} = \mathbf{f}_n^d + \epsilon_d, \quad \mathbf{f}_m^{s\epsilon} = \mathbf{f}_m^s + \epsilon_s, \quad (44)$$

where, With the similarities $\mathcal{S}(\mathbf{f}_m^s, \mathbf{f}_n^d)$ and $\mathcal{S}(\mathbf{f}_m^{s\epsilon}, \mathbf{f}_n^{d\epsilon})$, we can get two cross-view ranking lists $\{\mathcal{S}(\mathbf{f}_m^s, \mathbf{f}_n^d)\}$ and $\{\mathcal{S}(\mathbf{f}_m^{s\epsilon}, \mathbf{f}_n^{d\epsilon})\}$ for \mathbf{f}_m^s and $\mathbf{f}_m^{s\epsilon}$, which are denoted as $\mathcal{K}_s(\mathbf{f}_m^s)$ and $\mathcal{K}_s^{\epsilon}(\mathbf{f}_m^{s\epsilon})$.

The label of the k -th similar infrared instance in two ranking lists can be represented as:

$$\tilde{y}_{f_m^s}^{sd}[k] = y_{f_n^d}, \quad \mathbf{f}_n^d = \mathcal{K}_s(\mathbf{f}_m^s)[k] \quad (45)$$

$$\tilde{y}_{f_m^{s\epsilon}}^{sd}[k] = y_{f_n^{d\epsilon}}, \quad \mathbf{f}_n^{d\epsilon} = \mathcal{K}_s^{\epsilon}(\mathbf{f}_m^{s\epsilon})[k] \quad (46)$$

where $\tilde{y}_{f_m^s}^{sd}[k]$ and $\tilde{y}_{f_m^{s\epsilon}}^{sd}[k]$ are refined k -th cross-view labels of \mathbf{f}_m^s and $\mathbf{f}_m^{s\epsilon}$ through the ranking on cross-view initial features and perturbed features similarities.

So, we associate the cross-modality labels with the intersection of two label sets to investigate collaborative ranking consistency:

$$I_{f_m^s}(k) = \{\tilde{y}_{f_m^s}^{sd}[k] \cap \tilde{y}_{f_m^{s\epsilon}}^{sd}[k]\}_{p=1}^P, \quad (47)$$

where $I_{f_m^s}(k)$ records the samples with the same identity of top- k identity in instances from top-1 to top- X .

The reliable refined cross-view label of \mathbf{f}_m^s can be expressed by the label of maximum count in $I_{f_m^s}(k)$:

$$\tilde{y}_{f_m^s}^{cm} = \tilde{y}_{f_m^s}^{sd}[k], \quad k = \arg \max_k (|I_{f_m^s}(k)|, k \in [1, K]) \quad (48)$$

where $|\cdot|$ denotes the counting function. The $\arg \max$ operation traverses $I_{f_m^s}(k)$ and finds the labels with maximum number as cross-view refined labels.

Then, we convert the label list $\{\tilde{y}_{f_m^s}^{cm}, m \in [1, M]\}$ to the form of one-hot code matrix $\tilde{Y}^{cm} \in \mathbb{R}^{M \times N}$ by setting the column according to the refined labels to 1 and the rest to 0. Then, two initial and perturbed homogeneous initial P^{ss} and deep P_{ϵ}^{ss} similarity matrices are constructed to investigate intra-modality ranking consistency, enhancing the precision of refined cross-view pseudo labels by:

$$P^{ss}(m, m') = S(\mathbf{f}_m^s, \mathbf{f}_{m'}^s) \quad (49)$$

$$P_{\epsilon}^{ss}(m, m') = S(\mathbf{f}_m^{s\epsilon}, \mathbf{f}_{m'}^{s\epsilon}), \quad (50)$$

where $P_*^{ss} \in \mathbb{R}^{M \times M}$ represents the intra-view similarity structure.

In order to explore the intra-view initial and perturbed collaboration, we calculate the sum of $P^{ss}(m, m')$ and $P_{\epsilon}^{ss}(m, m')$ by:

$$P(m, m') = P^{ss}(m, m') + P_{\epsilon}^{ss}(m, m'), \quad (51)$$

where $P(m, m')$ indicates the consistency of initial and perturbed similarity matrix.

We keep the 5-max values of $P(m, m')$ in each row to 1 and set the rest to 0, acquiring the ranking relations. The process of intra-modality ranking smoothing is formulated as follows:

$$y^{cm} = P\tilde{y}^{cm}, \quad (52)$$

where $y^{cm} \in \mathbb{R}^{M \times N}$ is the final refined cross-view label matrix of satellite instance. In y^{cm} , the column number of the maximum value in each row is the refined label of samples.

TABLE I
COMPARISONS BETWEEN THE PROPOSED METHOD AND SOME STATE-OF-THE-ART METHODS ON THE UNIVERSITY-1652 DATASETS.

University-1652							
Model	Venue	Supervision Ratio	Params(M)	Drone→Satellite		Satellite→Drone	
				R@1	AP	R@1	AP
MuSe-Net[53]	PR'2024	100(%)	50.47	74.48	77.83	88.02	75.10
LPN[38]	TCSVT'2022	100(%)	62.39	75.93	79.14	86.45	74.49
Dai[54]	TIP'2023	100(%)	43.91	82.22	84.78	87.59	81.49
IFSs[35]	TGRS'2024	100(%)	-	86.06	88.08	91.44	85.73
MCCG[1]	TCSVT'2023	100(%)	56.65	89.40	91.07	95.01	89.93
SDPL[3]	TCSVT'2024	100(%)	42.56	90.16	91.64	93.58	89.45
CCR[33]	TCSVT'2024	100(%)	156.57	92.54	93.78	95.15	91.80
Sample4Geo[39]	ICCV'2023	100(%)	87.57	92.65	93.81	95.14	91.39
SRLN[36]	TGRS'2024	100(%)	193.03	92.70	93.77	95.14	91.97
DAC[4]	TCSVT'2024	100(%)	96.50	94.67	95.50	96.43	93.79
Ours	-	100(%)	28.59	92.02	93.36	95.57	91.27
Ours	-	0(%)	28.59	90.17	91.67	95.01	88.95

IV. EXPERIMENTAL RESULTS

A. Experimental Datasets and Evaluation Metrics

To evaluate the effectiveness of our proposed cross-view geo-localization framework, we conduct experiments on three benchmark datasets—University-1652 [9], SUES-200 [55], and DenseUAV [53]. These datasets present complementary challenges for multi-view image matching and retrieval.

University-1652 is a large-scale cross-view geo-localization dataset encompassing 1,652 locations from 72 universities worldwide. It contains multi-view images—drone, satellite, and ground-level. Of the total 1,652 buildings, 701 from 33 universities form the training set, while 951 from 39 different universities (with no geographic overlap) comprise the test set. As the first dataset to include drone-view for cross-view geo-localization, it facilitates matching across ground, drone, and satellite perspectives.

SUES-200 centers on altitude diversity in aerial imagery. It includes 200 distinct locations, split into 120 for training and 80 for testing. Each location provides one satellite image and aerial images taken at four altitudes (150m, 200m, 250m, and 300m), covering diverse environments such as urban areas, natural landscapes, and water bodies. *SUES-200* thus evaluates cross-view retrieval performance under varying flight heights, reflecting real-world UAV scenarios.

DenseUAV targets UAV self-positioning in low-altitude urban environments, featuring over 27,000 UAV and satellite images from 14 university campuses. It includes dense sampling, multi-scale satellite images, and varying altitudes (80m, 90m, 100m) across multiple temporal conditions. The training set consists of 6,768 UAV images and 13,536 satellite images, while the test set contains 2,331 UAV images and 4,662 satellite images, with no geographic overlap. *DenseUAV*'s challenges include cross-view matching, neighbor confusion, and spatial-temporal variation, making it a key benchmark for UAV-based localization in GPS-denied settings.

We evaluate the models using Recall@K (R@K) and Average Precision (AP). R@K measures the proportion of correct matches within the Top-*K* results, while AP balances precision

and recall. Model efficiency is assessed through parameter count, reflecting portability under resource constraints. Comparisons are made using the optimal model configurations for each method.

B. Implementation Details

We adopt a symmetric sampling strategy for selecting input images. A *ConvNeXt-Tiny* model, pre-trained on *ImageNet*, serves as the backbone for feature extraction, with a newly added classifier module initialized via the Kaiming method. During both training and testing, all input images are resized to $3 \times 384 \times 384$. We employ several data augmentation techniques, including random cropping, random horizontal flipping, and random rotation. The batch size is set to 64, and DBSCAN [10] is used to generate pseudo labels. For optimization, we use the SGD optimizer with an initial learning rate of 0.001, training the model for 30 epochs in total. All experiments are conducted under the PyTorch framework on an Ubuntu 22.04 system equipped with four NVIDIA RTX 4090 GPUs. Additionally, in the University-1652 and SUES-200 datasets, each location provides only a single satellite image; we therefore replicate each satellite feature 50 times for clustering purposes, leaving UAV features unchanged. In *DenseUAV*, we replicate UAV features four times at each altitude, and replicate the satellite features three times for each time point and altitude.

C. Comparison with State-of-the-art Methods

Results on University-1652: As shown in Table I, our proposed method, DMNIL, demonstrates outstanding performance, achieving competitive results without relying on paired matching data and labels. In both Drone→Satellite and Satellite→Drone settings, it attains R@1/AP of 90.17%/91.67% and 95.01%/88.95%, respectively, outperforming several fully supervised methods. Furthermore, we utilize unsupervised pre-trained weights and perform fine-tuning only on the ConvNeXt-Tiny backbone network with

TABLE II
COMPARISONS BETWEEN THE PROPOSED METHOD AND SOME STATE-OF-THE-ART METHODS ON THE SUES-200 DATASET.

SUES-200											
Model	Venue	Supervision Ratio	Paramars(M)	Drone→Satellite							
				150m		200m		250m		300m	
				R@1	AP	R@1	AP	R@1	AP	R@1	AP
LPN[38]	TCSVT'2022	100(%)	62.39	61.58	67.23	70.85	75.96	80.38	83.80	81.47	84.53
Vit[55]	TCSVT'2023	100(%)	172.20	59.32	64.93	62.30	67.24	71.35	75.49	77.17	80.67
MCCG[1]	TCSVT'2023	100(%)	56.65	82.22	85.47	89.38	91.41	93.82	95.04	95.07	96.20
SDPL[3]	TCSVT'2024	100(%)	42.56	82.95	85.82	92.73	94.07	96.05	96.69	97.83	98.05
CCR[33]	TCSVT'2024	100(%)	156.57	87.08	89.55	93.57	94.90	95.42	96.28	96.82	97.39
SRLN[36]	TGRS'2024	100(%)	193.03	89.90	91.90	94.32	95.65	95.92	96.79	96.37	97.21
Sample4Geo[39]	ICCV'2023	100(%)	87.57	92.60	94.00	97.38	97.81	98.28	98.64	99.18	99.36
DAC[4]	TCSVT'2024	100(%)	96.50	96.80	97.54	97.48	97.97	98.20	98.62	97.58	98.14
MEAN[2]	arXiv'2024	100(%)	36.50	95.50	96.46	98.38	98.72	98.95	99.17	99.52	99.63
Ours	-	100(%)	28.59	94.00	95.21	97.83	98.88	99.14	95.44	99.25	99.39
Ours [†]	-	0(%)	28.59	82.60	85.60	90.48	92.28	94.33	95.44	96.78	97.42
Ours [‡]	-	0(%)	28.59	87.00	89.20	93.98	95.11	96.50	97.23	97.23	97.86
Ours*	-	0(%)	28.59	90.98	92.66	95.03	96.14	97.45	98.03	98.23	98.64

Satellite→Drone											
Model	Venue	Supervision Ratio	Paramars(M)	Satellite→Drone							
				150m		200m		250m		300m	
				R@1	AP	R@1	AP	R@1	AP	R@1	AP
LPN[38]	TCSVT'2022	100(%)	62.39	83.75	83.75	83.75	83.75	83.75	83.75	83.75	83.75
Vit[55]	TCSVT'2023	100(%)	172.20	82.50	58.95	85.00	62.56	88.75	69.96	96.25	84.16
CCR[33]	TCSVT'2024	100(%)	156.57	92.50	88.54	97.50	95.22	97.50	97.10	97.50	97.49
Sample4Geo[39]	ICCV'2023	100(%)	87.57	92.60	94.00	97.38	97.81	98.28	98.64	99.18	99.36
MCCG[1]	TCSVT'2023	100(%)	56.65	93.75	89.72	93.75	92.21	96.25	96.14	98.75	96.64
SDPL[3]	TCSVT'2024	100(%)	42.56	93.75	83.75	96.25	92.42	97.50	95.65	96.25	96.17
SRLN[36]	TGRS'2024	100(%)	193.03	93.75	93.01	97.50	95.08	97.50	96.52	97.50	96.71
DAC[4]	TCSVT'2024	100(%)	96.50	97.50	94.06	98.75	96.66	98.75	98.09	98.75	97.87
MEAN[2]	arXiv'2024	100(%)	36.50	97.50	94.75	100.00	97.09	100.00	98.28	100.00	99.21
Ours	-	100(%)	28.59	97.50	92.71	97.50	97.43	100.00	98.98	98.75	98.25
Ours [†]	-	0(%)	28.59	91.25	81.28	97.50	90.62	98.75	94.74	97.50	96.17
Ours [‡]	-	0(%)	28.59	95.00	85.46	97.50	92.72	100.00	95.43	100.00	96.39
Ours*	-	0(%)	28.59	96.25	90.05	97.50	94.80	98.75	96.82	98.75	97.33

labeled data. This approach results in performance improvements of 1.85%/1.69% and 0.56%/2.32% in the two settings, approaching or surpassing the performance of most current state-of-the-art supervised models. Additionally, the model has a parameter count of only 28.59M, demonstrating high computational efficiency and low resource requirements.

Results on SUES-200: As shown in Table II, † denotes the results obtained by training the model in an unsupervised manner on the university-1652 dataset and testing it on the SUES-200 dataset. ‡ represents the results of training the model in an unsupervised manner using the university-1652 dataset. * refers to the results obtained by fine-tuning the model, which was pre-trained using †, on the SUES-200 dataset for 1 epoch in an unsupervised manner. As shown in Table II, our method demonstrates strong performance in domain adaptation and transfer, even without the need for re-training. By transferring the training weights from the University-1652 dataset, we achieve impressive results, surpassing some supervised methods, all without utilizing any paired data or label information. Furthermore, when retraining with our method on the SUES-200 dataset, our approach outperforms most state-of-the-art supervised methods, such as SRLN, CCR, and SDPL, across all four heights in two

different settings. Additionally, when the training weights from the University-1652 dataset are used, followed by fine-tuning the model for one epoch on the SUES-200 dataset, we observe even better performance, highlighting the effectiveness of our method in model fine-tuning and optimization. Finally, when fine-tuning a model retrained on the SUES-200 dataset using label signals, we achieve optimal results, demonstrating performance on par with or even exceeding current state-of-the-art supervised methods, underscoring the superiority of our approach in transfer learning, adaptation to various height settings, and model optimization.

Results on Cross-Domain Generalization Performance: In cross-view geo-localization, cross-domain adaptability is a critical metric for evaluating the generalization capability of a model, especially when the training and testing datasets exhibit significant differences. To evaluate the transferability of our proposed model, we conducted experiments by training on the University-1652 dataset and testing on the SUES-200 dataset. As shown in Table III, our method demonstrates superior generalization performance under the challenging University-1652→SUES-200 and Satellite→Drone cross-domain settings. Remarkably, our model achieves state-of-the-art results without any supervision (0% supervision ratio) while utiliz-

TABLE III
COMPARISONS BETWEEN THE PROPOSED METHOD AND STATE-OF-THE-ART METHODS IN CROSS-DOMAIN EVALUATION.

University-1652→SUES-200											
Model	Venue	Supervision Ratio	Paramars(M)	Drone→Satellite							
				150m		200m		250m		300m	
				R@1	AP	R@1	AP	R@1	AP	R@1	AP
MCCG[1]	TCSVT'2023	100(%)	56.65	57.62	62.80	66.83	71.60	74.25	78.35	82.55	85.27
Sample4Geo[39]	ICCV'2023	100(%)	87.57	70.05	74.93	80.68	83.90	87.35	89.72	90.03	91.91
DAC[4]	TCSVT'2024	100(%)	96.50	76.65	80.56	86.45	89.00	92.95	94.18	94.53	95.45
CAMP[34]	TGRS'2024	100(%)	91.40	78.90	82.38	86.83	89.28	91.95	93.63	95.68	96.65
MEAN[2]	arXiv'2024	100(%)	36.50	81.73	87.72	89.05	91.00	92.13	93.60	94.63	95.76
Ours	-	0(%)	28.59	82.60	85.60	90.48	92.28	94.33	95.44	96.78	97.42
Satellite→Drone											
Model	Venue	Supervision Ratio	Paramars(M)	Satellite→Drone							
				150m		200m		250m		300m	
				R@1	AP	R@1	AP	R@1	AP	R@1	AP
MCCG[1]	TCSVT'2023	100(%)	56.65	61.25	53.51	82.50	67.06	81.25	74.99	87.50	80.20
Sample4Geo[39]	ICCV'2023	100(%)	87.57	83.75	73.83	91.25	83.42	93.75	89.07	93.75	90.66
DAC[4]	TCSVT'2024	100(%)	96.50	87.50	79.87	96.25	88.98	95.00	92.81	96.25	94.00
CAMP[34]	TGRS'2024	100(%)	91.40	87.50	78.98	95.00	87.05	95.00	91.05	96.25	93.44
MEAN[2]	arXiv'2024	100(%)	36.50	91.25	81.50	96.25	89.55	95.00	92.36	96.25	94.32
Ours	-	0(%)	28.59	91.25	81.28	97.50	90.62	98.75	94.74	97.50	96.17

ing significantly fewer parameters (28.59M). For University-1652→SUES-200, our method outperforms all fully supervised baselines across most distance thresholds. At 300m, we attain R@1/AP of 96.78%/97.42%, surpassing the previous best results (CAMP) by 1.10% and 0.77%, respectively. Notably, even at lower altitude (150m), our model achieves R@1 of 82.60%, outperforming MEAN and CAMP, highlighting its robustness to domain shifts. In the Satellite→Drone scenario, our method further exhibits exceptional generalization. At 250m, we achieve R@1/AP of 98.75%/94.74%, improving upon the second-best method (DAC) by 3.75% and 1.93%, respectively. The consistent performance gains across varying distances (e.g., 97.50% R@1 at 300m) underscore the effectiveness of our unsupervised paradigm in mitigating domain discrepancies. These results validate that our approach not only reduces dependency on labeled data but also enhances cross-domain adaptability through efficient feature learning. The lightweight architecture (28.59M parameters) further ensures practical applicability in resource-constrained scenarios, setting a new benchmark for unsupervised cross-view geolocalization.

Results on DenseUAV: The DenseUAV dataset presents a highly challenging scenario due to its densely sampled nature, where neighboring images are easily confused, making cross-view matching particularly difficult. Furthermore, the inclusion of multi-scale satellite imagery and UAV images taken at different altitudes adds another layer of complexity, often leading to unstable retrieval performance in conventional methods. However, As shown in Table IV, our approach demonstrates exceptional performance under both fully supervised (100% supervision ratio) and zero-supervision (0% supervision ratio) settings. In the fully supervised case, our method achieves an impressive 99.61% R@1 at 90m altitude and 99.49% R@5 at 100m, closely matching or even surpassing the current state-of-the-art method (MEAN). More notably, under zero

supervision, our method still achieves 73.79% R@1 and 90.69% R@5 at All height, significantly outperforming some fully supervised approaches, proving its strong generalization and robustness. These results highlight our method’s ability to effectively address the challenge of neighboring image confusion and provide reliable UAV self-localization in GPS-denied environments.

D. Ablation Studies

To comprehensively evaluate the rationale behind our proposed method, we conducted an ablation study on the University-1652 dataset. We systematically analyzed the impact of each proposed module and explored their effectiveness in different configurations to better understand their contributions to the cross-geographic view matching task. The experimental results are shown in Table V.

Backbone: Basic Feature Extraction Capability. The Backbone refers to the performance of the ConvNeXt-Tiny network without training, serving as a direct feature extractor. As shown in Table V, its performance is significantly limited, achieving an R@1 of only 9.55% and 35.24%, and an AP of 11.88% and 13.20% for the Drone → Satellite and Satellite → Drone tasks, respectively. This result confirms that the backbone alone lacks the capability to extract discriminative features, highlighting the necessity of additional learning mechanisms.

Baseline: Dual-Path Contrastive Learning for Feature Optimization. Incorporating a Baseline model with dual-path cluster-based contrastive learning significantly enhances feature discrimination. The R@1 values rise to 71.06% and 81.31%, while AP improves to 74.91% and 65.26%. These improvements demonstrate that contrastive learning strengthens intra-view feature discrimination but remains insufficient for capturing cross-view consistency.

Dynamic Hierarchical Memory Learning (DHML): Enhancing Global and Local Consistency. To further address consistency between cross-views, we propose DHML. This module

TABLE IV
COMPARISONS BETWEEN THE PROPOSED METHOD AND SOME STATE-OF-THE-ART METHODS ON THE DENSEUAV DATASETS.

DenseUAV											
Model	Venue	Supervision Ratio	Paramars(M)	All height		80m		90m		100m	
				R@1	R@5	R@1	R@5	R@1	R@5	R@1	R@5
ConvNext-Tiny[37]	TIP'2024	100(%)	30.10	60.23	81.94	-	-	-	-	-	-
Sample4Geo[39]	ICCV'2023	100(%)	87.57	80.57	96.53	80.57	96.53	86.87	98.71	91.38	99.74
CAMP[34]	TGRS'2024	100(%)	91.40	88.72	97.76	76.45	96.01	84.81	99.23	89.19	99.23
DAC[4]	TCSVT'2024	100(%)	96.50	84.47	96.53	80.92	97.04	85.32	98.71	85.46	99.10
MEAN[2]	arXiv'2024	100(%)	36.50	90.18	97.86	78.76	97.04	85.33	99.10	89.32	98.97
Ours	-	100(%)	28.59	86.31	97.81	86.10	98.46	88.93	99.61	90.35	99.49
Ours	-	0(%)	28.59	73.79	90.69	73.10	92.92	74.65	95.37	75.03	95.50

TABLE V
THE INFLUENCE OF EACH COMPONENT ON THE PERFORMANCE OF PROPOSED DMNIL.

Setting		University-1652						
		Drone→Satellite		Satellite→Drone				
Backbone	Baseline	DHML	ICEL	PLE	R@1	AP	R@1	AP
✓					9.55	11.88	35.24	13.20
✓	✓				71.06	74.91	81.31	65.26
✓	✓	✓			84.03	86.41	90.44	82.74
✓	✓		✓		74.48	77.96	89.87	74.37
✓	✓	✓	✓		86.13	88.31	94.01	82.97
✓	✓	✓	✓	✓	90.17	91.67	95.01	88.95

effectively mines hierarchical feature dependencies and improves structural alignment. Consequently, R@1 increases to 84.03% and 48.72%, while AP reaches 86.41% and 82.74%. This confirms that DHML significantly strengthens feature robustness across different views.

Information Consistency Evolution Learning (ICEL): Leveraging Cross-View Associations. Although DHML improves feature consistency, it is still constrained to within-view optimizations. Therefore, we propose ICEL to explicitly model cross-view dependencies. ICEL enables mutual feature refinement across views, boosting R@1 to 86.13% and 51.04%, with AP increasing to 88.31% and 82.97%. These results further confirm the effectiveness of ICEL, showing that it significantly enhances information consistency in cross-geographic view matching tasks, improving the overall model performance.

Pseudo-Label Enhancement (PLE): Refining Feature Learning with Robust Labels. To mitigate pseudo-label noise caused by clustering, we apply PLE to improve label reliability. After incorporating PLE, our final model achieves state-of-the-art performance, with R@1 increasing to 90.17% and 95.01%, and AP reaching 91.67% and 88.95%. This confirms that refining pseudo-label quality significantly enhances the final model's effectiveness in cross-geographic view matching.

The ablation study comprehensively validates the impact of each component in the proposed DMNIL framework. Starting from the backbone, which lacks discriminative capacity, to the baseline method leveraging contrastive learning, followed by the enhancements brought by DHML for global-local consistency, ICEL for cross-view feature association, and finally PLE for pseudo-label refinement, each module plays a crucial role

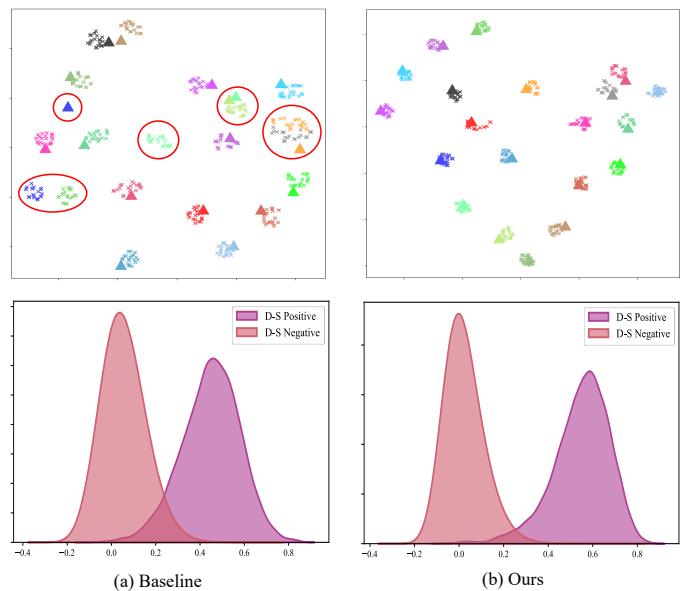


Fig. 4. The first row presents the t-SNE visualization, while the second row illustrates the similarity distribution for randomly selected geographic locations. In the t-SNE visualization, each color represents a distinct location, where 'x' markers correspond to the drone viewpoint, and the triangles indicate the satellite perspective of the same location.

in improving performance. The results demonstrate that our approach systematically enhances feature learning, leading to superior matching performance on University-1652.

E. Visualization

Feature space and similarity distribution. To further illustrate the effectiveness of our method, we perform feature space (t-SNE[56] map) and similarity distribution visualization for DMNIL, as presented in Fig 4. Comparing (a) Baseline and (b) Our Method, it is evident that our approach enhances the clustering of cross-view positive samples, effectively bringing the drone and satellite representations of the same location closer together. Additionally, the separation between different locations is more distinct, indicating better feature discriminability. The second row shows the similarity distribution between drone-satellite positive and negative pairs. Our method

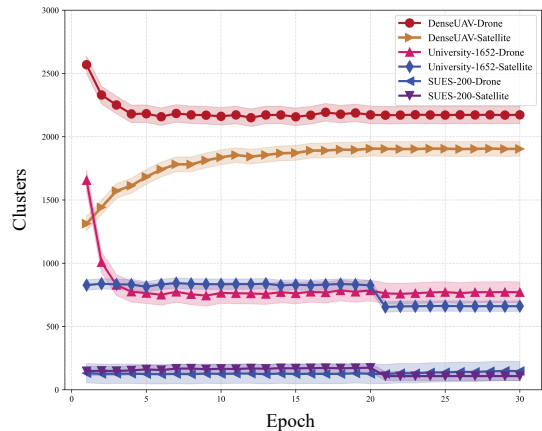


Fig. 5. Cluster analysis across different epochs for various datasets. The plot shows the number of clusters for DenseUAV, University-1652, and SUES-200 datasets, each for both drone and satellite data.

demonstrates a clearer distinction between positive and negative pairs, with a reduced overlap between distributions, which suggests improved cross-view matching and reduced feature ambiguity. This highlights the effectiveness of our approach in addressing viewpoint discrepancies across geographic perspectives.

Cluster analysis. To validate the efficacy of our method, as shown in Fig. 5, we illustrate the evolution of cluster counts across epochs for three cross-view datasets. In the DenseUAV dataset (2,255 locations), satellite images exhibit significant clustering fluctuations during the early training stages, due to low intra-class discriminability and weak cross-view correlations. In contrast, the University-1652 dataset (701 locations) demonstrates greater UAV image clustering instability, while satellite image clusters stabilize more rapidly in the initial epochs. The SUES-200 dataset (1,200 locations), with its smaller data size and simpler distribution, exhibits minimal early-stage variation and stabilizes faster than larger datasets. As training progresses, the cluster counts across all datasets gradually converge toward the ground-truth location counts, despite initial inter-class confusion. This process validates our model’s ability to progressively learn discriminative representations.

Retrieval results. To demonstrate the effectiveness of the DMNIL, we present retrieval results on the University-1652 and DenseUAV dataset in Fig. 6 and Fig. 7. Green borders indicate correct matches, while red borders denote errors, showing that DMNIL significantly improves retrieval accuracy.

In the University-1652 dataset, the drone-to-satellite task presents drone queries in the left panel and retrieved satellite images in the right panel. Since each location has only one satellite image, DMNIL consistently achieves Top-1 accuracy, demonstrating its effectiveness. For satellite-to-drone retrieval, DMNIL accurately matches satellite queries to the corresponding drone images (green borders), showcasing its robust cross-view geo-localization capability and strong feature consistency across perspectives.



Fig. 6. Top-6 Retrieval Results of the Proposed DMNIL on the University-1652 Dataset.

In the DenseUAV dataset, the retrieval task is more challenging due to dense sampling, multi-scale satellite imagery, and temporal variations, increasing the difficulty of cross-view matching. Since each location corresponds to multiple satellite images, the model must handle neighbor confusion effectively. In the Drone \rightarrow Satellite task, despite variations in UAV altitude and satellite scale, our method accurately extracts spatial-geographic features, achieving high retrieval accuracy and significantly reducing mismatches. Compared to University-1652, DenseUAV better reflects real-world UAV localization scenarios, where our method demonstrates strong cross-view retrieval performance, effectively distinguishing dense regions and enhancing model robustness.

V. CONCLUSION

This paper investigates a highly valuable and challenging task namely cross-view geo-localization based on UAV-view, aiming to reduce reliance on costly paired matching data. To address the challenges posed by cross-view discrepancies, we propose a lightweight unsupervised framework for UAV-view geo-localization, incorporating dynamic hierarchical memory learning and information consistency evolution learning. This framework unifies intra-view and cross-view feature representations in a high-dimensional space, further revealing

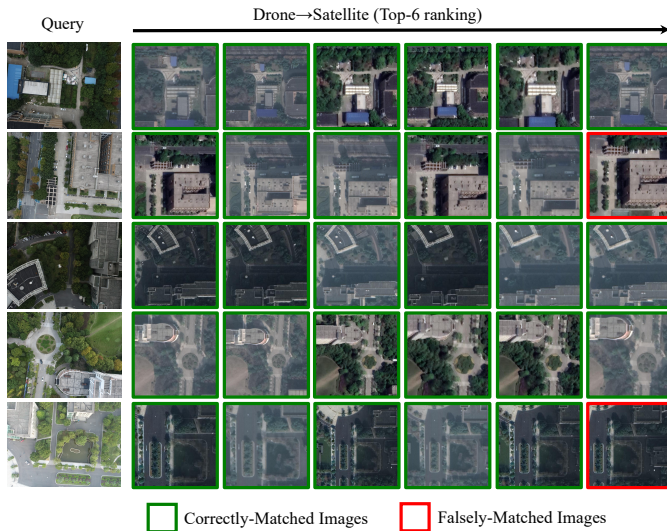


Fig. 7. Top-6 Retrieval Results of the Proposed DMNIL on the DenseUAV Dataset.

their intrinsic correlations and cross-view mapping patterns. Experiments conducted on three public benchmark datasets demonstrate that our method, even without relying on paired matching data, surpasses some fully supervised counterparts while maintaining a compact network design. Furthermore, when adapted to the fully supervised setting, our approach achieves performance comparable to state-of-the-art models, further validating its effectiveness. These results enhance the practical applicability of UAV-view geo-localization and provide new opportunities for real-world deployment.

REFERENCES

- [1] T. Shen, Y. Wei, L. Kang, S. Wan, and Y.-H. Yang, "MCCG: A convnext-based multiple-classifier method for cross-view geo-localization," *IEEE Transactions on Circuits and Systems for Video Technology*, vol. 34, no. 3, pp. 1456–1468, 2023.
- [2] Z. Chen, Z.-X. Yang, and H.-J. Rong, "Multi-level embedding and alignment network with consistency and invariance learning for cross-view geo-localization," *arXiv preprint arXiv:2412.14819*, 2024.
- [3] Q. Chen, T. Wang, Z. Yang, H. Li, R. Lu, Y. Sun, B. Zheng, and C. Yan, "SDPL: Shifting-dense partition learning for UAV-view geo-localization," *IEEE Transactions on Circuits and Systems for Video Technology*, vol. 34, no. 11, pp. 11 810–11 824, 2024.
- [4] P. Xia, Y. Wan, Z. Zheng, Y. Zhang, and J. Deng, "Enhancing cross-view geo-localization with domain alignment and scene consistency," *IEEE Transactions on Circuits and Systems for Video Technology*, pp. 1–12, 2024.
- [5] H. Li, C. Xu, W. Yang, H. Yu, and G.-S. Xia, "Learning cross-view visual geo-localization without ground truth," *arXiv preprint arXiv:2403.12702*, 2024.
- [6] J. Yin, X. Zhang, Z. Ma, J. Guo, and Y. Liu, "A real-time memory updating strategy for unsupervised person re-identification," *IEEE Transactions on Image Processing*, vol. 32, pp. 2309–2321, 2023.
- [7] Z. Liu, H. Mao, C.-Y. Wu, C. Feichtenhofer, T. Darrell, and S. Xie, "A convnet for the 2020s," in *IEEE/CVF Conference on Computer Vision and Pattern Recognition (CVPR)*, 2022, pp. 11 976–11 986.
- [8] J. Deng, W. Dong, R. Socher, L.-J. Li, K. Li, and L. Fei-Fei, "Imagenet: A large-scale hierarchical image database," in *Proceedings of the IEEE Conference on Computer Vision and Pattern Recognition (CVPR)*. Ieee, 2009, pp. 248–255.
- [9] Z. Zheng, Y. Wei, and Y. Yang, "University-1652: A multi-view multi-source benchmark for drone-based geo-localization," *ACM Multimedia*, no. 9, pp. 1395–1403, 2020.
- [10] L. Wei, S. Zhang, W. Gao, and Q. Tian, "Person transfer gan to bridge domain gap for person re-identification," in *Proceedings of the IEEE Conference on Computer Vision and Pattern Recognition (CVPR)*, June 2018.
- [11] Z. Zheng, L. Zheng, and Y. Yang, "A discriminatively learned cnn embedding for person reidentification," *ACM transactions on multimedia computing, communications, and applications (TOMM)*, vol. 14, no. 1, pp. 1–20, 2017.
- [12] Y. Sun, Y. Chen, X. Wang, and X. Tang, "Deep learning face representation by joint identification-verification," *Advances in neural information processing systems*, vol. 27, 2014.
- [13] L. Zheng, L. Shen, L. Tian, S. Wang, J. Wang, and Q. Tian, "Scalable person re-identification: A benchmark," in *Proceedings of the IEEE international conference on computer vision*, 2015, pp. 1116–1124.
- [14] Z. Wu, Y. Xiong, S. X. Yu, and D. Lin, "Unsupervised feature learning via non-parametric instance discrimination," in *Proceedings of the IEEE conference on computer vision and pattern recognition*, 2018, pp. 3733–3742.
- [15] C. Hu and G. H. Lee, "Feature representation learning for unsupervised cross-domain image retrieval," in *Proceedings of the European Conference on Computer Vision (ECCV)*, 2022.
- [16] B. Yang, J. Chen, and M. Ye, "Towards grand unified representation learning for unsupervised visible-infrared person re-identification," in *Proceedings of the IEEE/CVF International Conference on Computer Vision (ICCV)*, October 2023, pp. 11 069–11 079.
- [17] Y. Fang, P.-T. Yap, W. Lin, H. Zhu, and M. Liu, "Source-free unsupervised domain adaptation: A survey," *Neural Networks*, p. 106230, 2024.
- [18] Z. Chen, Z. Zhang, X. Tan, Y. Qu, and Y. Xie, "Unveiling the power of clip in unsupervised visible-infrared person re-identification," in *Proceedings of the 31st ACM International Conference on Multimedia*, 2023, pp. 3667–3675.
- [19] Z. Wu and M. Ye, "Unsupervised visible-infrared person re-identification via progressive graph matching and alternate learning," in *Proceedings of the IEEE/CVF Conference on Computer Vision and Pattern Recognition (CVPR)*, June 2023, pp. 9548–9558.
- [20] Z. Pang, C. Wang, L. Zhao, Y. Liu, and G. Sharma, "Cross-modality hierarchical clustering and refinement for unsupervised visible-infrared person re-identification," in *IEEE Transactions on Circuits and Systems for Video Technology*, vol. 34, no. 4, 2024, pp. 2706–2718.
- [21] H. Chen, Y. Wang, B. Lagadeec, A. Dantcheva, and F. Bremond, "Joint generative and contrastive learning for unsupervised person re-identification," in *Proceedings of the IEEE/CVF Conference on Computer Vision and Pattern Recognition (CVPR)*, June 2021, pp. 2004–2013.
- [22] D. H. Pham, A. D. Nguyen, and H. N. Nguyen, "Gan-based data augmentation and pseudo-label refinement with holistic features for unsupervised domain adaptation person re-identification," *Knowledge-Based Systems*, vol. 288, p. 111471, 2024.
- [23] H. Chen, Y. Wang, B. Lagadeec, A. Dantcheva, and F. Bremond, "Learning invariance from generated variance for unsupervised person re-identification," *IEEE Transactions on Pattern Analysis and Machine Intelligence*, vol. 45, no. 6, pp. 7494–7508, 2023.
- [24] Y. Zheng, S. Tang, G. Teng, Y. Ge, K. Liu, J. Qin, D. Qi, and D. Chen, "Online pseudo label generation by hierarchical cluster dynamics for adaptive person re-identification," in *Proceedings of the IEEE/CVF International Conference on Computer Vision (ICCV)*, October 2021, pp. 8371–8381.
- [25] Y. Cho, W. J. Kim, S. Hong, and S.-E. Yoon, "Part-based pseudo label refinement for unsupervised person re-identification," in *Proceedings of the IEEE/CVF Conference on Computer Vision and Pattern Recognition (CVPR)*, June 2022, pp. 7308–7318.
- [26] B. Sha, B. Li, T. Chen, J. Fan, and T. Sheng, "Rethinking pseudo-label-based unsupervised person re-id with hierarchical prototype-based graph," in *Proceedings of the 31st ACM International Conference on Multimedia*, 2023, pp. 2090–2100.
- [27] I. Goodfellow, J. Pouget-Abadie, M. Mirza, B. Xu, D. Warde-Farley, S. Ozair, A. Courville, and Y. Bengio, "Generative adversarial nets," *Advances in neural information processing systems*, vol. 27, 2014.
- [28] M. Ester, H.-P. Kriegel, J. Sander, X. Xu *et al.*, "A density-based algorithm for discovering clusters in large spatial databases with noise," in *kdd*, vol. 96, no. 34, 1996, pp. 226–231.
- [29] J. MacQueen *et al.*, "Some methods for classification and analysis of multivariate observations," in *Proceedings of the fifth Berkeley symposium on mathematical statistics and probability*, vol. 1, no. 14, 1967, pp. 281–297.

- [30] G. Li, M. Qian, and G.-S. Xia, "Unleashing unlabeled data: A paradigm for cross-view geo-localization," in *Proceedings of the IEEE/CVF Conference on Computer Vision and Pattern Recognition (CVPR)*, June 2024, pp. 16719–16729.
- [31] Z. Dai, G. Wang, W. Yuan, S. Zhu, and P. Tan, "Cluster contrast for unsupervised person re-identification," in *Proceedings of the Asian conference on computer vision*, 2022, pp. 1142–1160.
- [32] B. Yang, M. Ye, J. Chen, and Z. Wu, "Augmented dual-contrastive aggregation learning for unsupervised visible-infrared person re-identification," in *ACM MM*, 2022, p. 2843–2851.
- [33] H. Du, J. He, and Y. Zhao, "CCR: A counterfactual causal reasoning-based method for cross-view geo-localization," *IEEE Transactions on Circuits and Systems for Video Technology*, vol. 34, no. 11, pp. 11630–11643, 2024.
- [34] Q. Wu, Y. Wan, Z. Zheng, Y. Zhang, G. Wang, and Z. Zhao, "CAMP: Across-view geo-localization method using contrastive attributes mining and position-aware partitioning," *IEEE Transactions on Geoscience and Remote Sensing*, vol. 62, pp. 1–14, 2024.
- [35] F. Ge, Y. Zhang, Y. Liu, G. Wang, S. Coleman, D. Kerr, and L. Wang, "Multibranch joint representation learning based on information fusion strategy for cross-view geo-localization," *IEEE Transactions on Geoscience and Remote Sensing*, vol. 62, pp. 1–16, 2024.
- [36] H. Lv, H. Zhu, R. Zhu, F. Wu, C. Wang, M. Cai, and K. Zhang, "Direction-guided multi-scale feature fusion network for geo-localization," *IEEE Transactions on Geoscience and Remote Sensing*, vol. 62, pp. 1–13, 2024.
- [37] M. Dai, E. Zheng, Z. Feng, L. Qi, J. Zhuang, and W. Yang, "Vision-based uav self-positioning in low-altitude urban environments," *IEEE Transactions on Image Processing*, vol. 33, pp. 493–508, 2024.
- [38] T. Wang, Z. Zheng, C. Yan, J. Zhang, Y. Sun, B. Zheng, and Y. Yang, "Each part matters: Local patterns facilitate cross-view geo-localization," *IEEE Transactions on Circuits and Systems for Video Technology*, vol. 32, no. 2, pp. 867–879, 2021.
- [39] F. Deuser, K. Habel, and N. Oswald, "Sample4Geo: Hard negative sampling for cross-view geo-localisation," in *IEEE/CVF International Conference on Computer Vision (ICCV)*, 2023, pp. 16847–16856.
- [40] X. Zhang, X. Li, W. Sultani, C. Chen, and S. Wshah, "GeoDTR+: Toward generic cross-view geolocalization via geometric disentanglement," *IEEE Transactions on Pattern Analysis and Machine Intelligence*, vol. 46, no. 12, pp. 10419–10433, 2024.
- [41] S. Hu, M. Feng, R. M. H. Nguyen, and G. H. Lee, "Cvm-net: Cross-view matching network for image-based ground-to-aerial geo-localization," in *Proceedings of the IEEE Conference on Computer Vision and Pattern Recognition (CVPR)*, June 2018.
- [42] S. Zhu, M. Shah, and C. Chen, "TransGeo: Transformer is all you need for cross-view image geo-localization," in *IEEE/CVF Conference on Computer Vision and Pattern Recognition (CVPR)*, 2022, pp. 1162–1171.
- [43] X. Zhang, X. Li, W. Sultani, Y. Zhou, and S. Wshah, "Cross-view geo-localization via learning disentangled geometric layout correspondence," in *Proceedings of the AAAI Conference on Artificial Intelligence*, vol. 37, no. 3, 2023, pp. 3480–3488.
- [44] J.-Y. Zhu, T. Park, P. Isola, and A. A. Efros, "Unpaired image-to-image translation using cycle-consistent adversarial networks," in *Proceedings of the IEEE International Conference on Computer Vision (ICCV)*, Oct 2017.
- [45] M. Caron, P. Bojanowski, A. Joulin, and M. Douze, "Deep clustering for unsupervised learning of visual features," in *Proceedings of the European Conference on Computer Vision (ECCV)*, September 2018.
- [46] M. Caron, I. Misra, J. Mairal, P. Goyal, P. Bojanowski, and A. Joulin, "Unsupervised learning of visual features by contrasting cluster assignments," *Advances in neural information processing systems*, vol. 33, pp. 9912–9924, 2020.
- [47] B. Yang, J. Chen, and M. Ye, "Shallow-deep collaborative learning for unsupervised visible-infrared person re-identification," in *Proceedings of the IEEE/CVF Conference on Computer Vision and Pattern Recognition*, 2024, pp. 16870–16879.
- [48] Z. Wu, Y. Xiong, S. X. Yu, and D. Lin, "Unsupervised feature learning via non-parametric instance discrimination," in *Proceedings of the IEEE Conference on Computer Vision and Pattern Recognition (CVPR)*, June 2018.
- [49] P. Bachman, R. D. Hjelm, and W. Buchwalter, "Learning representations by maximizing mutual information across views," *Advances in neural information processing systems*, vol. 32, 2019.
- [50] K. He, H. Fan, Y. Wu, S. Xie, and R. Girshick, "Momentum contrast for unsupervised visual representation learning," in *Proceedings of the IEEE/CVF Conference on Computer Vision and Pattern Recognition (CVPR)*, June 2020.
- [51] T. Chen, S. Kornblith, M. Norouzi, and G. Hinton, "A simple framework for contrastive learning of visual representations," in *International conference on machine learning*. PMLR, 2020, pp. 1597–1607.
- [52] B. Yang, J. Chen, C. Chen, and M. Ye, "Dual consistency-constrained learning for unsupervised visible-infrared person re-identification," *IEEE Transactions on Information Forensics and Security*, 2023.
- [53] T. Wang, Z. Zheng, Y. Sun, C. Yan, Y. Yang, and T.-S. Chua, "Multiple-environment self-adaptive network for aerial-view geo-localization," *Pattern Recognition*, vol. 152, p. 110363, 2024.
- [54] M. Dai, E. Zheng, Z. Feng, L. Qi, J. Zhuang, and W. Yang, "Vision-based UAV self-positioning in low-altitude urban environments," *IEEE Transactions on Image Processing*, vol. 33, pp. 493–508, 2024.
- [55] R. Zhu, L. Yin, M. Yang, F. Wu, Y. Yang, and W. Hu, "SUES-200: A multi-height multi-scene cross-view image benchmark across drone and satellite," *IEEE Transactions on Circuits and Systems for Video Technology*, vol. 33, no. 9, pp. 4825–4839, 2023.
- [56] L. Van der Maaten and G. Hinton, "Visualizing data using t-SNE," *Journal of machine learning research*, vol. 9, no. 11, pp. 2579–2605, 2008.